

## Materials Science

## Engineering the Si/Al ratio of MWW zeolites for propylene/propane separation

Zhongliang Tang<sup>#</sup>, Qing Xu<sup>#</sup>, Yue Wu, Xinghao Shi, Xinyu Zhu, Xiaoling Liu<sup>\*</sup>, Jun Wang<sup>\*</sup> & Yu Zhou<sup>\*</sup>

State Key Laboratory of Materials-Oriented Chemical Engineering, College of Chemical Engineering, Nanjing Tech University, Nanjing 211816, China

<sup>#</sup>Contributed equally to this work.

<sup>\*</sup>Corresponding authors (emails: [liuxiaoling@njtech.edu.cn](mailto:liuxiaoling@njtech.edu.cn) (Xiaoling Liu); [junwang@njtech.edu.cn](mailto:junwang@njtech.edu.cn) (Jun Wang); [njtzhouyu@njtech.edu.cn](mailto:njtzhouyu@njtech.edu.cn) (Yu Zhou))

Received 8 October 2025; Revised 31 October 2025; Accepted 3 November 2025; Published online 5 November 2025

**Abstract:** Propylene/propane (C<sub>3</sub>H<sub>6</sub>/C<sub>3</sub>H<sub>8</sub>) separation is critical to the petrochemical industry but remains highly energy-consuming. Adsorption-based strategies provide a promising energy-efficient alternative, yet developing adsorbents combining both high capacity and selectivity is challenging due to the nearly identical physicochemical properties of C<sub>3</sub>H<sub>6</sub> and C<sub>3</sub>H<sub>8</sub>. Here, we systematically investigated MCM-22 zeolites (MWW topology) with varying Si/Al ratios (9.6–36.5) for C<sub>3</sub>H<sub>6</sub>/C<sub>3</sub>H<sub>8</sub> separation. Gas adsorption isotherms, cyclic sorption tests, and dynamic breakthrough experiments revealed that the Si/Al ratio significantly regulated the separation performance. Remarkably, MCM-22(30) with a moderate Si/Al ratio of 18.7 achieved the best performance, achieving a high C<sub>3</sub>H<sub>6</sub> uptake (6.28 mmol g<sup>-1</sup>) at 298 K and 1 bar (1 bar = 10<sup>5</sup> Pa), with an exceptional ideal adsorption solution theory (IAST) C<sub>3</sub>H<sub>6</sub>/C<sub>3</sub>H<sub>8</sub> (50/50, v/v) selectivity exceeding 3000, while maintaining favorable regenerability and structural stability over multiple cycles. Breakthrough experiments further demonstrated the superior dynamic separation efficiency of MCM-22(30) compared with its higher- or lower-Si/Al counterparts.

**Keywords:** propylene purification, adsorption and separation, zeolites, hydrothermal synthesis, structural modulation

### INTRODUCTION

Propylene (C<sub>3</sub>H<sub>6</sub>) is one important industrial chemical serving as a key feedstock for producing polypropylene, acrylonitrile, propylene oxide, and numerous other high-value chemicals [1–4]. The growing demand for polymer-grade propylene necessitates its efficient separation from propane (C<sub>3</sub>H<sub>8</sub>) [2,5]. At present, cryogenic distillation remains the dominant industrial technology; however, it is among the most energy-intensive processes in the chemical industry due to the extremely close boiling points of C<sub>3</sub>H<sub>6</sub> and C<sub>3</sub>H<sub>8</sub> (−47.6 °C vs. −42.1 °C) [1,4,6]. This substantial energy burden has driven increasing interest in the development of alternative, energy-saving separation technologies [7].

Among the emerging approaches, adsorption-based separation has gained growing attention owing to its low energy demand, mild operating conditions, and facile regenerability [8–10]. The major challenge, however, lies in designing adsorbents that simultaneously achieve high adsorption capacity and selectivity, given the nearly identical physicochemical properties and comparable molecular sizes of C<sub>3</sub>H<sub>6</sub> (0.468 × 0.457 nm) and C<sub>3</sub>H<sub>8</sub> (0.502 × 0.502 nm) [11–13]. Various porous materials have been investigated for

$C_3H_6/C_3H_8$  separation, such as metal-organic frameworks (MOFs), covalent organic frameworks (COFs), and carbon-based materials, and zeolite [13–17]. In particular, MOFs have demonstrated exceptional performance for  $C_3H_6/C_3H_8$  separation because of their structural diversity and high tunability with respect to pore dimensions and functionality [2,5]. For example,  $Cu_{10}O_{13}$ -based MOF with a water nanotube within the channel exhibited a high  $C_3H_6/C_3H_8$  selectivity of 1570 at 298 K and 1 bar [6]. Among these materials, zeolites are a family of low-cost inorganic crystals with excellent thermal and hydrothermal stability, well-defined pore architectures, and tunable chemical composition. Owing to these virtues, zeolites have been widely applied as adsorbents in industry, and in particular, LiX have been utilized in air separation to produce high-purity  $O_2$  and  $N_2$  via pressure swing adsorption (PSA) [18].

The ordered channel systems of zeolites enable molecular discrimination through subtle differences in size, shape, and framework interactions [11,19]. In general, small-pore zeolites (e.g., 8-membered-ring frameworks) exhibit high  $C_3H_6/C_3H_8$  selectivity via molecular sieving or diffusion control, as their pore apertures are comparable to the kinetic diameters of  $C_3H_6$  and  $C_3H_8$  [20–23]. For example, pure-silica ITQ-3, chabazite (CHA), and high silica ZSM-58 (DDR) with 8-membered-ring channels have demonstrated distinct diffusion rates for  $C_3H_6$  and  $C_3H_8$ , evidencing strong kinetic selectivity toward  $C_3H_6$  [22,23]. However, the application of small pore zeolites is often hindered by their low adsorption capacities and severe diffusion limitations [24–26]. In contrast, large-pore zeolites provide higher uptake and faster mass transfer but generally suffer from poor selectivity because their pore apertures are much larger than the molecular dimensions of  $C_3H_6$  and  $C_3H_8$  [27–29]. Therefore, achieving an optimal balance between pore confinement, adsorption strength, and molecular accessibility remains a key challenge.

The adsorption and separation behavior of zeolites is strongly influenced by topology, Si/Al ratio, morphology, and overall composition [30–33]. High-silica zeolites are often preferred to mitigate pore blockage caused by olefin oligomerization, making Si/Al ratio engineering one of the most effective strategies for tailoring adsorption performance [21,22,31,34]. Among the diverse zeolite families, the MWW-type framework has recently emerged as a promising candidate for physical adsorbent [35,36]. With its two-dimensional sinusoidal 10-membered-ring channels and large super-cages accessible through 12-membered-ring opening, the layered MWW structure integrates the benefits of both small and large pore zeolites, generating a multi-functional adsorption environment [37,38]. Nevertheless, systematic studies on MWW zeolites for  $C_3H_6/C_3H_8$  separation remain limited. In particular, the influence of the Si/Al ratio on adsorptive separation performance, cycling stability, and dynamic breakthrough behavior has yet to be thoroughly elucidated.

Here, we synthesized a series of MCM-22 zeolites with tunable Si/Al ratios (9.6–36.5) and systematically evaluated their  $C_3H_6/C_3H_8$  separation performance. A combination of static gas adsorption, cyclic adsorption-desorption, and breakthrough experiments was employed to elucidate the influence of framework composition on separation efficiency. Systematic investigations revealed that the moderate Si/Al ratio delivers both high adsorption capacity and selectivity. The optimal adsorbent MCM-22(30) with a moderate Si/Al ratio of 18.7 exhibited the best performance, achieving a  $C_3H_6$  uptake of  $6.28 \text{ mmol g}^{-1}$  and a  $C_3H_6/C_3H_8$  selectivity above 3000 for an equimolar mixture at 298 K. Moreover, MCM-22(30) maintained structural stability and separation efficiency after multiple sorption cycles. Breakthrough tests further confirmed the superior dynamic selectivity of MCM-22(30) for  $C_3H_6$  over  $C_3H_8$ .

**Table 1** Textural properties

Sample	Element content <sup>a</sup> (wt%)			Si/Al	Na/Al	Chemical formula	Crystal system	Space group	$S_{\text{BET}}^b$ ( $\text{m}^2 \text{g}^{-1}$ )	$V^c$ ( $\text{cm}^3 \text{g}^{-1}$ )	$D^d$ (nm)
	Na	Al	Si								
MCM-22(15)	0.34	3.9	39.1	9.6	0.10	$[\text{Na}_{0.68}\text{H}_{6.12}][\text{Al}_{6.8}\text{Si}_{65.2}\text{O}_{144}]$	Hexagonal	$P6/mmm$	546	0.23	0.83
MCM-22(30)	0.14	2.0	40.0	18.7	0.08	$[\text{Na}_{0.29}\text{H}_{3.41}][\text{Al}_{3.7}\text{Si}_{68.3}\text{O}_{144}]$	Hexagonal	$P6/mmm$	594	0.26	0.90
MCM-22(60)	0.03	1.1	41.9	36.5	0.03	$[\text{Na}_{0.06}\text{H}_{1.84}][\text{Al}_{1.9}\text{Si}_{70.1}\text{O}_{144}]$	Hexagonal	$P6/mmm$	550	0.23	0.88

<sup>a</sup> Measured by XRF. <sup>b</sup> BET surface area. <sup>c</sup> Total pore volume. <sup>d</sup> Average pore width.

## RESULTS AND DISCUSSION

### Synthesis and characterization

Three MWW-type zeolites with variable Si/Al ratios were synthesized hydrothermally and designated as MCM-22(*n*), where *n* = 15, 30, and 60 denotes the theoretical Si/Al ratio in the gel. The experimental detected Si/Al ratios were 9.6, 18.7, and 36.5 for *n* = 15, 30, and 60, respectively (Table 1). The chemical compositions of MCM-22(15), MCM-22(30), and MCM-22(60) were  $[\text{Na}_{0.68}\text{H}_{6.12}][\text{Al}_{6.8}\text{Si}_{65.2}\text{O}_{144}]$ ,  $[\text{Na}_{0.29}\text{H}_{3.41}][\text{Al}_{3.7}\text{Si}_{68.3}\text{O}_{144}]$ , and  $[\text{Na}_{0.06}\text{H}_{1.84}][\text{Al}_{1.9}\text{Si}_{70.1}\text{O}_{144}]$ , respectively. The experimental measured values were consistently lower than the nominal gel ratios, which can be attributed to the different reactivity and solubility of silica and aluminum species during crystallization [39]. Particularly, the  $\text{Al}(\text{OH})_4^-$  anion effectively compensates the framework negative charge and is more readily incorporated into the zeolite framework, resulting in a reduced Si/Al ratio. All the X-ray diffraction (XRD) patterns exhibited the characteristic reflections of the MWW topology (Figure 1a). MCM-22(*n*) crystallized in a hexagonal system with the space group  $P6/mmm$ . Prominent peaks in the low-angle region ( $2\theta \approx 6^\circ\text{--}10^\circ$ ) correspond to layered structural reflections (e.g., (002), (100), and (hydrophobicity)), while multiple reflections in the mid-angle region ( $2\theta \approx 12^\circ\text{--}13^\circ$  and  $22^\circ\text{--}25^\circ$ ) are assigned to the ordered framework planes [40,41]. The similarity in diffraction peak positions across the three samples confirms that the MWW framework was successfully formed irrespective of Si/Al ratio. No impurity phases were detected, indicating high phase purity. Among the samples, MCM-22(30) displayed the sharpest and most intense reflections, implying the highest crystallinity and layer stacking order. Thermogravimetric (TG) analysis revealed gradual weight loss upon heating from room temperature to 800 °C (Figure 1b). All samples showed an initial weight loss below 200 °C, corresponding to the removal of physically adsorbed water (9.0%, 6.7%, and 3.6% for *n* = 15, 30, and 60, respectively). A subsequent minor loss up to ~600 °C (1.7%, 0.9%, and 0.45%) was mainly assigned to water desorption from the condensation of residual framework hydroxyl groups. The total weight loss decreased as the Si/Al ratio increased. Specially, MCM-22(15) with the lowest Si/Al ratio exhibited the largest overall loss (10.7% up to ~600 °C), followed by MCM-22(30) (7.6%), while MCM-22(60) presented the smallest (4.4%). This trend reflects the enhanced hydrophobicity at higher Si/Al ratio, which reduces the amount of adsorbed water and hydroxyl species.

The textural properties of MCM-22(*n*) were determined by nitrogen sorption experiment at 77 K. All samples displayed type I+IV isotherms (Figure 1c), indicative of predominant microporosity along with minor mesoporosity [42,43]. The steep uptake at low relative pressures corresponds to micropore filling,

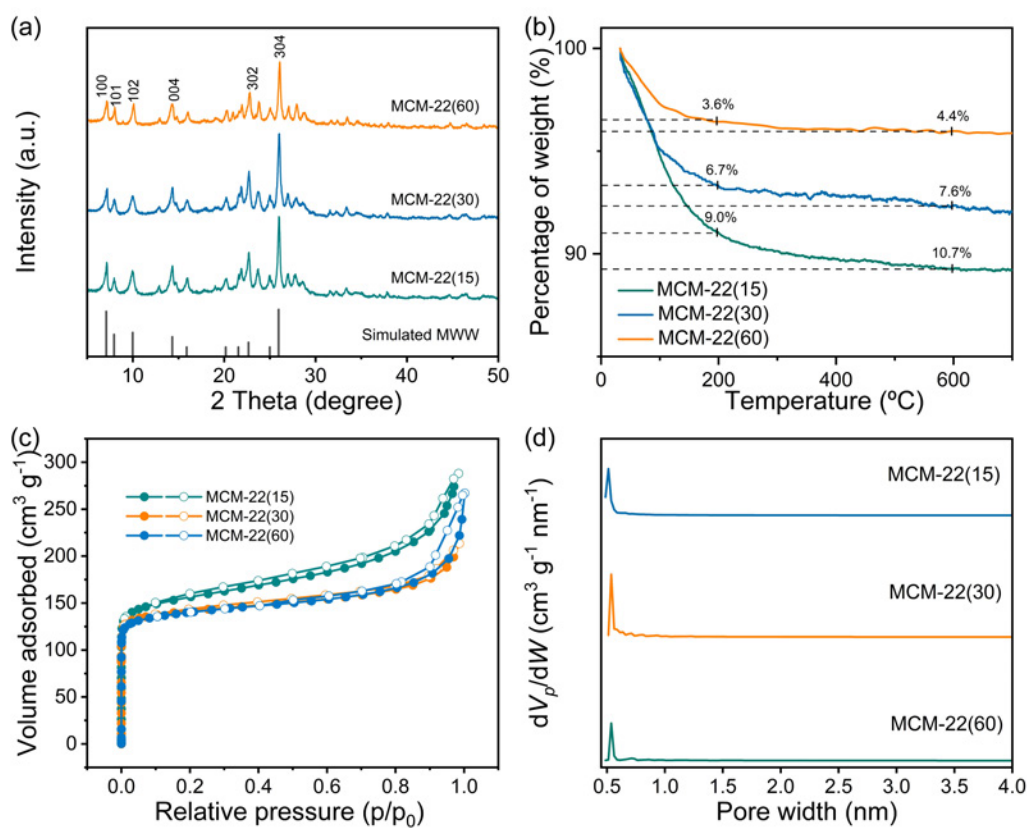


**Figure 1** (a) XRD patterns, (b) TG profiles, (c)  $N_2$  sorption isotherms, and (d) pore size distribution curves of MCM-22(*n*).

whereas the slight hysteresis loop at higher relative pressures reflects secondary mesopores formed by interparticle packing, which is further reflected by the pore size distribution curves (Figure 1d). The corresponding surface areas and pore volumes are listed in Table 1. All of them showed high surface area and pore volume, with the values of  $546 \text{ m}^2 \text{ g}^{-1}$  and  $0.23 \text{ cm}^3 \text{ g}^{-1}$  for MCM-22(15),  $594 \text{ m}^2 \text{ g}^{-1}$  and  $0.26 \text{ cm}^3 \text{ g}^{-1}$  for MCM-22(30), and  $550 \text{ m}^2 \text{ g}^{-1}$  and  $0.23 \text{ cm}^3 \text{ g}^{-1}$  for MCM-22(60). The overall similarity of the isotherms indicates that the intrinsic microporosity of the MWW framework was preserved, while minor variations in surface area like arise from subtle differences in crystal size and stacking.

The surface wettability of MCM-22(*n*) was assessed by a water contact angle test (Figure 2a–c). The water contact angles of MCM-22(15), MCM-22(30), and MCM-22(60) were  $19.1^\circ$ ,  $28.8^\circ$ , and  $53.9^\circ$ , respectively, indicating that increasing the Si/Al ratio reduces hydrophilicity due to a lower density of surface hydroxyl groups. Scanning electron microscope (SEM) images of MCM-22(*n*) exhibited typical aggregated platelet-like morphologies characteristic of MWW structure (Figure 2d–g). The primary particles were nanosheets with the size from 100 to 300 nm (Figure 2). They were randomly packed with each other to give aggregations at the micrometer level. MCM-22(15) showed relatively compact aggregates with tightly stacked layers, whereas MCM-22(30) and MCM-22(60) exhibited more open assemblies with discernible inter-crystalline voids and aggregation density without altering the primary platelet morphology [39,41]. The Fourier transform infrared (FT-IR) spectra of MCM-22(*n*) displayed the typical vibrational features of the MWW framework (Figure S1). Broad bands at  $3430\text{--}3440 \text{ cm}^{-1}$  are assigned to O–H stretching vibrations of

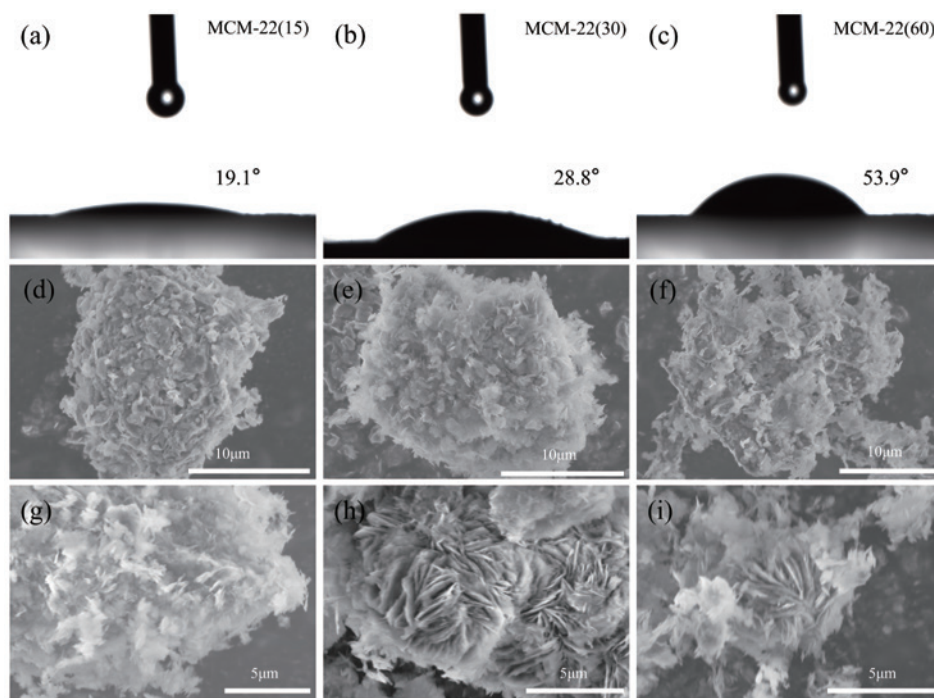


**Figure 2** Water contact angles of (a) MCM-22(15), (b) MCM-22(30), and (c) MCM-22(60). SEM images of (d, g) MCM-22(15), (e, h) MCM-22(30), and (f, i) MCM-22(60).

surface hydroxyl groups and adsorbed water, with bending modes near  $1636\text{--}1660\text{ cm}^{-1}$  [44–46]. Strong absorption at  $\sim 1090\text{--}1050\text{ cm}^{-1}$ , together with bands at  $791\text{--}768$  and  $447\text{--}444\text{ cm}^{-1}$ , corresponds to the asymmetric and symmetric Si–O–Si stretching and bending vibrations [47]. The characteristic band at  $\sim 617\text{--}610\text{ cm}^{-1}$  comes from the double six-membered-ring (D6R) units, a fingerprint of the MWW structure [44,48]. All three samples showed similar spectra, confirming structural uniformity [40], while the intensity of the hydroxyl-related bands decreased with increasing Si/Al ratio, consistent with the enhanced hydrophobicity of high-silica samples.

### Gas adsorption

Single-component adsorption isotherms of  $\text{C}_3\text{H}_6$  and  $\text{C}_3\text{H}_8$  on MCM-22(*n*) samples were collected using a volumetric adsorption analyzer (Figure 3). The  $\text{C}_3\text{H}_6$  adsorption isotherms at 298 K (Figure 3a) exhibited typical type I+IV behavior, characterized by a steep at low relative pressures [49]. MCM-22(15) showed a gradual increase in uptake with increasing pressure, reaching a  $\text{C}_3\text{H}_6$  uptake of  $4.45\text{ mmol g}^{-1}$  at 1 bar. As the Si/Al ratio increased to 30, the adsorption capacity significantly improved over the entire pressure range, attributable to the higher crystallinity and larger surface area of MCM-22(30). A maximum  $\text{C}_3\text{H}_6$  uptake of  $6.28\text{ mmol g}^{-1}$  was reached at 1 bar (1 bar =  $10^5\text{ Pa}$ ). However, at a higher Si/Al ratio of 60, the sample exhibited a reduced uptake ( $3.95\text{ mmol g}^{-1}$ ). Considering that MCM-22(60) has almost same textural properties to MCM-22(15) ( $546$  vs.  $550\text{ m}^2\text{ g}^{-1}$  and  $0.23$  vs.  $0.23\text{ cm}^3\text{ g}^{-1}$ ), the decline can be assigned to the decreased framework Al density and weakened electrostatic field strength, which diminish the host-guest

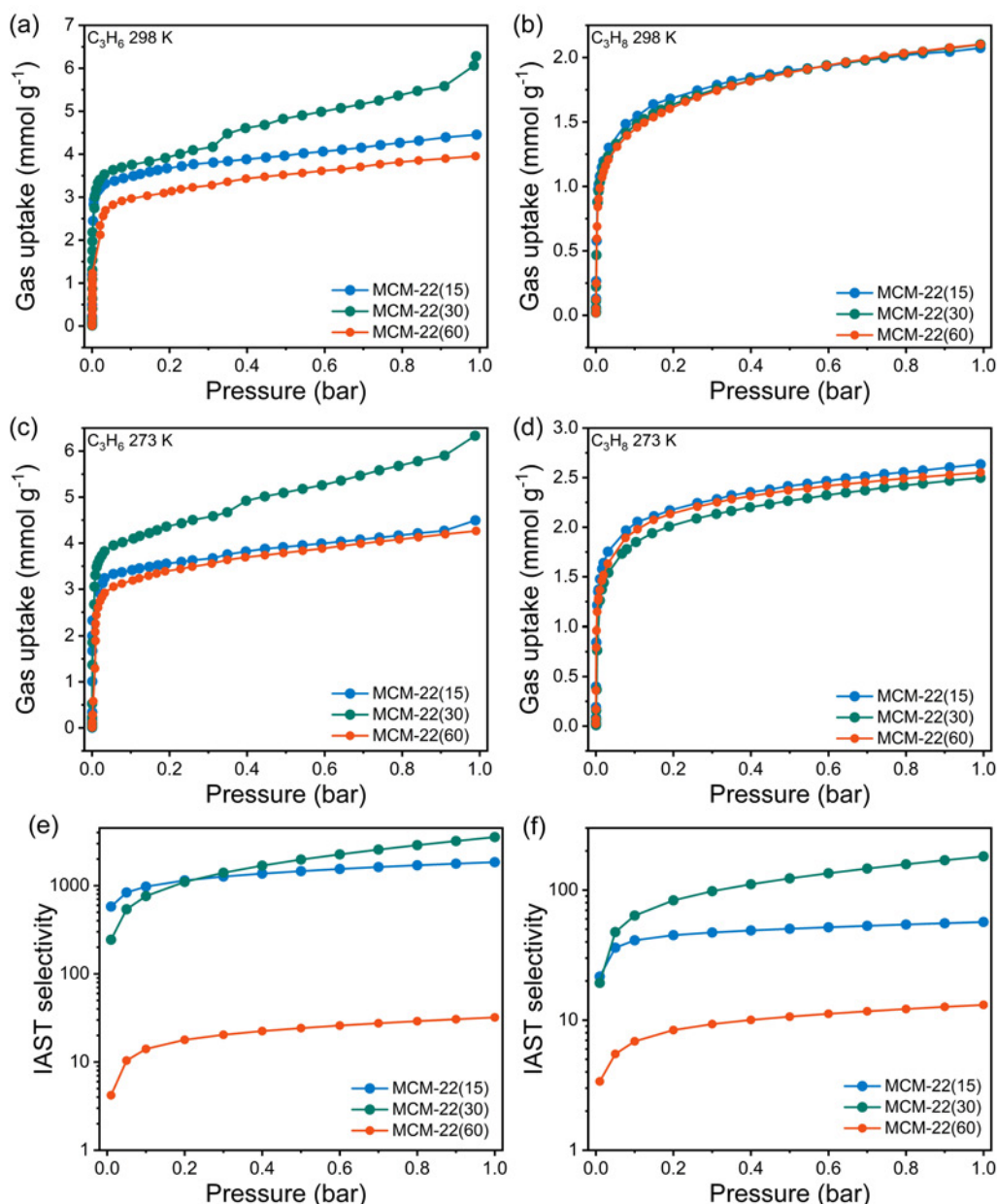


**Figure 3** (a)  $C_3H_6$  and (b)  $C_3H_8$  adsorption isotherms of MCM-22( $n$ ) at 298 K up to 1 bar. (c)  $C_3H_6$  and (d)  $C_3H_8$  adsorption isotherms of MCM-22( $n$ ) at 273 K up to 1 bar. IAST predictions of  $C_3H_6/C_3H_8$  (50/50, v/v) selectivities of MCM-22( $n$ ) at (e) 298 K and (f) 273 K.

interactions between  $C_3H_6$  molecules and the zeolites channels [31,50]. The  $C_3H_8$  adsorption isotherms at 298 K (Figure 3b) display similar shapes for all three samples, with uptake capacities of 2.07, 2.10, and 2.10  $mmol\ g^{-1}$  at 1 bar for  $n = 15, 30,$  and  $60,$  respectively (Table S1). The initial uptakes at low relative pressures are evident, but the overall adsorption of  $C_3H_8$  is much weaker than that of  $C_3H_6$ , suggesting a weaker interaction between  $C_3H_8$  molecules and the MCM-22 framework.

These  $C_3H_6$  and  $C_3H_8$  adsorption isotherms were fitted by using different equations. High agreement was achieved by using the Dual-Langmuir (DL) equation [30], indicating the presence of two distinct adsorption

sites for both  $C_3H_6$  and  $C_3H_8$  on MCM-22(*n*) (Figures S2–S13). The fitted parameters revealed that both the saturated capacities and equilibrium constants of  $C_3H_6$  were larger than those of  $C_3H_8$ , confirming the stronger affinity of MCM-22 for  $C_3H_6$  adsorption. Based on these fitted parameters, the ideal adsorption solution theory (IAST) was applied to predict the  $C_3H_6/C_3H_8$  selectivity for the separation of an equimolar (50/50, v/v) mixture (Figure 3e) [51]. The calculated  $C_3H_6/C_3H_8$  selectivities increased with pressure for all samples. Among them, MCM-22(15) exhibited a selectivity of 1846 at 1 bar, which further increased to 3553 for MCM-22(30), demonstrating that increasing the Si/Al ratio enhances both  $C_3H_6$  uptake and  $C_3H_6/C_3H_8$  selectivity (Table S1). Further increasing the Si/Al ratio to 60, however, reduced the  $C_3H_6/C_3H_8$  selectivities due to the weakened  $C_3H_6$ -zeolite interaction [50]. The selective adsorption performance of MCM-22(30) is superior or at least comparable to reported  $C_3H_6$ -selective porous materials with similar pore sizes [6,20,52,53].

The temperature-dependent adsorption behavior was further investigated at 273 K (Figure 3c and d). The isotherm profiles of both  $C_3H_6$  and  $C_3H_8$  remained similar to those at 298 K. For  $C_3H_6$  adsorption (Figure 3c), only minor variations were observed between 273 and 298 K, with uptakes of 4.49 vs. 4.45 mmol g<sup>-1</sup> for MCM-22(15), 6.33 vs. 6.28 mmol g<sup>-1</sup> for MCM-22(30), and 4.27 vs. 3.95 mmol g<sup>-1</sup> for MCM-22(60). This suggests that  $C_3H_6$  adsorption is only weakly temperature-dependent. In contrast,  $C_3H_8$  adsorption increased noticeably at the lower temperature (Figure 3d), with uptakes of 2.63 vs. 2.07 mmol g<sup>-1</sup> for MCM-22(15), 2.50 vs. 2.10 mmol g<sup>-1</sup> for MCM-22(30), and 2.55 vs. 2.10 mmol g<sup>-1</sup> for MCM-22(60), reflecting a stronger thermodynamic driving force for  $C_3H_8$  adsorption at 273 K. Consequently, the calculated  $C_3H_6/C_3H_8$  (50/50, v/v) selectivities decreased at 273 K, with MCM-22(30) maintaining the highest value of 181, followed by MCM-22(15) (57) and MCM-22(60) (13) (Figure 3f). Considering that industrial separations are generally performed near ambient temperature, the weak temperature dependence of  $C_3H_6$  adsorption on MCM-22(30) highlights its suitability for practical applications.

Five-cycle adsorption–desorption recyclability tests confirmed good recyclability (Figure 4). After each run, the samples were reactivated under vacuum activated before reuse. For  $C_3H_6$  adsorption, the isotherm shapes remained nearly identical throughout the cycles (Figure 4a–c). A moderate decline in uptake occurred between the first and second runs, particularly for MCM-22(15), where the uptake decreased from 4.45 to 2.57 mmol g<sup>-1</sup>. Thereafter, the capacities stabilized with negligible loss ever after the 5th cycle. MCM-22(30) retained a high  $C_3H_6$  uptake (> 5 mmol g<sup>-1</sup> in the 5th run), outperforming both MCM-22(15) (2.53 mmol g<sup>-1</sup>) and MCM-22(60) (3.37 mmol g<sup>-1</sup>) (Table S1). In contrast, the  $C_3H_8$  adsorption isotherms showed almost overlapping profiles across all cycles (Figure 4b), confirming good reversibility and stability. The  $C_3H_8$  capacities in the 5th run were nearly identical to those in the 1st run for all samples, suggesting a negligible influence of Si/Al ratio on cycling  $C_3H_8$  adsorption. The evolution of  $C_3H_6/C_3H_8$  selectivity during cycling further highlights the importance of the Si/Al ratio. For MCM-22(15), selectivity drastically decreased from 1846 in the 1st run to 3.6 in the 2nd run, and stabilized around 2 thereafter (Figure S14 and Table S1). At a high Si/Al ratio (MCM-22(60)), selectivity declined gradually over successive cycles, reaching only 2.7 after the 5th run (Figure S15 and Table S1). In contrast, MCM-22(30) maintained superior performance, with selectivity decreasing modestly from 3553 to 478 in the 2nd run and remaining above 300 in subsequent cycles (Figure S16 and Table S1). The sustained high  $C_3H_6$  uptake and  $C_3H_6/C_3H_8$  selectivity for MCM-22(30) confirms its favorable recycling adsorption-desorption operation.

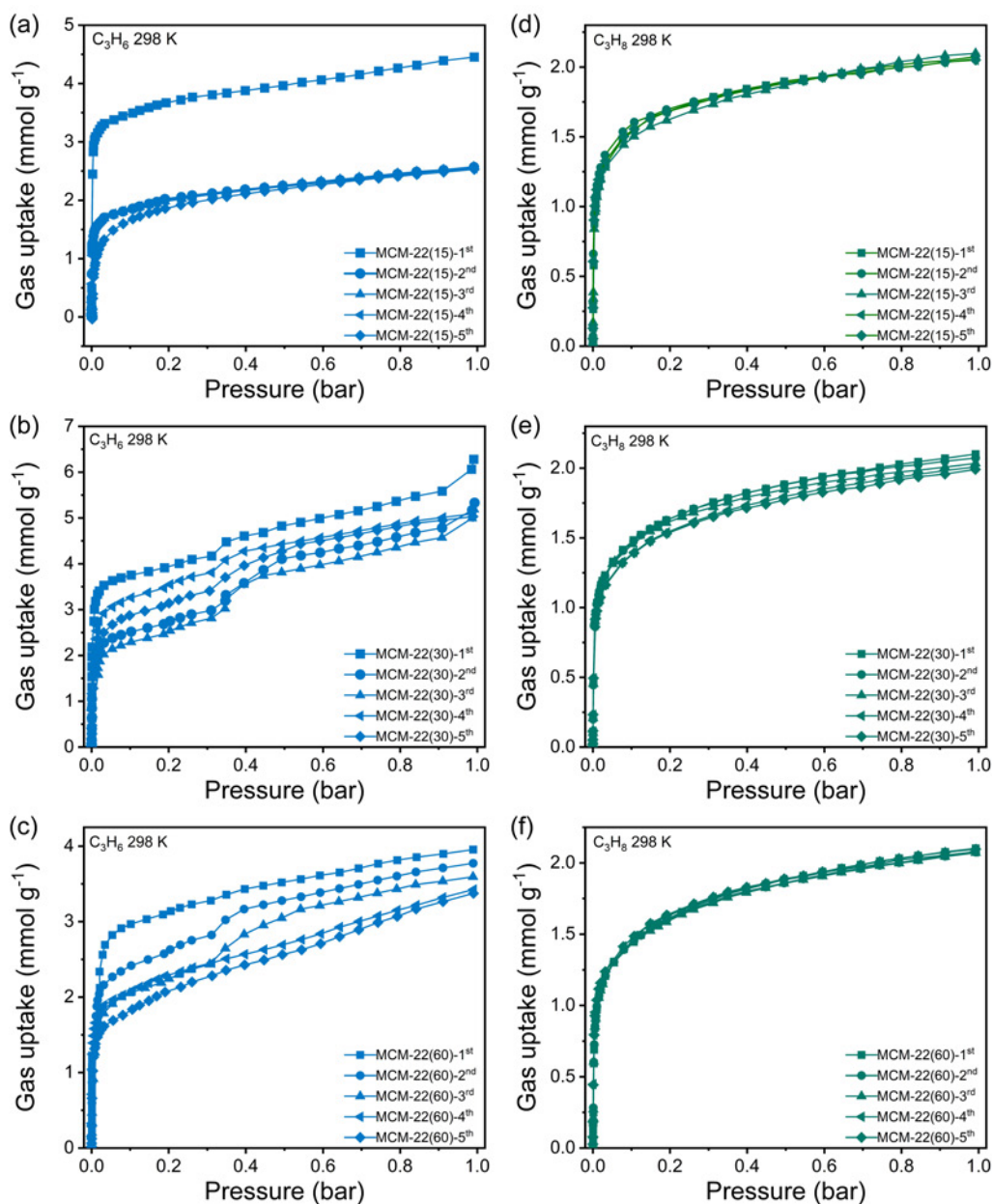


**Figure 4** Recycling adsorption isotherms of  $C_3H_6$  on (a) MCM-22(15), (b) MCM-22(30), (c) MCM-22(60), and  $C_3H_8$  on (d) MCM-22(15), (e) MCM-22(30), (f) MCM-22(60).

### Structure of spent MWW zeolites

Structural characterizations were conducted on the spent MCM-22(*n*) recovered after the 5th run of  $C_3H_6$  adsorption, denoted as MCM-22(*n*)-5th. Their XRD patterns retained the characteristic reflections of the MWW topology (Figure 5a), corroborating that the crystalline structure was preserved after repeated sorption cycles. The sharp and well-defined diffraction peaks were observed in the low- and moderate-angle regions, with negligible position shifts or the emergence of impurity phases. The slight attenuation of diffraction

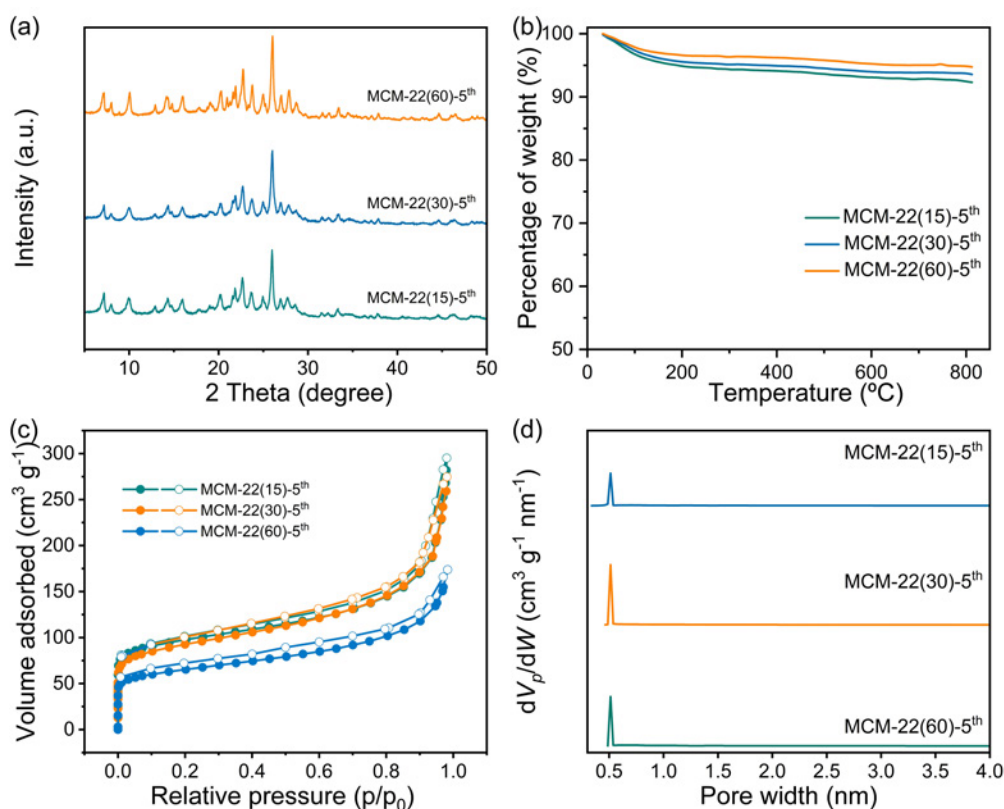


**Figure 5** (a) XRD patterns, (b) TG profiles, (c)  $N_2$  sorption isotherms, and (d) pore size distribution curves of spent MCM-22( $n$ )-5th.

intensities for the spent samples can be attributed to residual organic species, mainly the propylene oligomers, remaining within the channels, which reduce electron-density contrast between the framework walls and pores [2,54].

TG profiles of MCM-22( $n$ )-5th showed two distinct weight-loss regions (Figure 5b). The first below 200 °C corresponds to desorption of physisorbed water, while the second (200–600 °C) arises from decomposition of residue organics. The initial weight loss followed the sequence 5.1% ( $n = 15$ ) > 4.5% ( $n = 30$ ) > 3.4% ( $n = 60$ ), consistent with the improved hydrophobicity at higher Si/Al ratios. Compared with the fresh samples, all spent zeolites showed reduced initial weight loss, further indicating that residual organics increased surface hydrophobicity. The second weight loss (1.8%, 1.6%, and 1.4%) was larger than that of the pristine materials, validating the presence of adsorbed hydrocarbon residues from  $C_3H_6$  sorption process. Elemental analysis of MCM-22( $n$ )-5th was performed to quantify the hydrocarbon residue in Table S2. The carbon residue content of MCM-22(15) was higher than that of MCM-22(30) and MCM-22(60), consistent with the results of TG.

$N_2$  sorption isotherms (Figure 5c) of MCM-22( $n$ )-5th maintained the type IV features of the fresh samples, with significant micropore uptake at low  $p/p_0$  and a gradual rise at higher pressure. However, the uptakes at low relative pressures were notably reduced, while those at high pressure ( $p/p_0 > 0.8$ ) increased, suggesting the formation of secondary mesopores [44]. MCM-22(15)-5th exhibited the most pronounced decline in surface area and pore volume (546 to 234  $m^2 g^{-1}$  and 0.23 to 0.11  $cm^3 g^{-1}$ ) (Figure 5c, d, and Table S3),

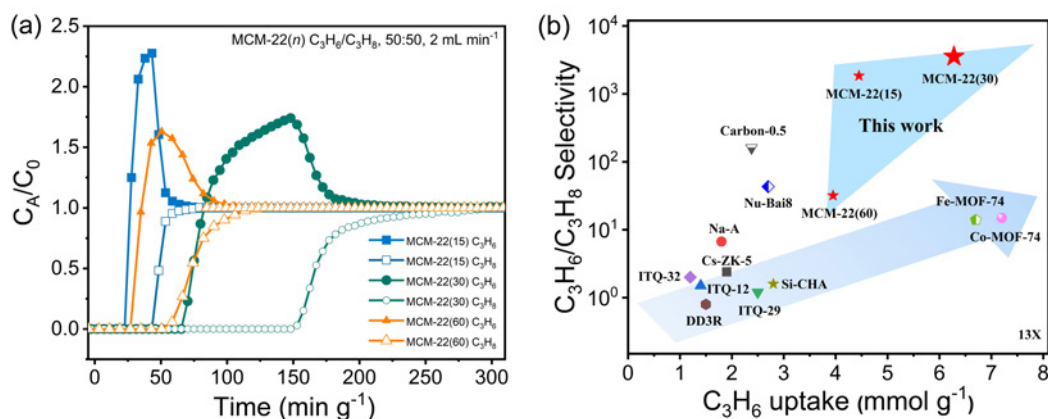


**Figure 6** (a) Breakthrough curves for the separation of a  $C_3H_6/C_3H_8$  (50/50, v/v) mixture on MCM-22(*n*). (b) Comparison of IAST  $C_3H_6/C_3H_8$  (50/50, v/v) selectivity and  $C_3H_6$  uptake ( $\text{mmol g}^{-1}$ ) of MCM-22(*n*) with advanced  $C_3H_6$ -selective materials at 298 K and 1 bar.

indicating partial pore blockage by retained organics. Increasing the Si/Al ratio mitigated these losses. MCM-22(30)-5th maintained  $358 \text{ m}^2 \text{ g}^{-1}$  surface area and  $0.17 \text{ cm}^3 \text{ g}^{-1}$  pore volume (Figure 5c, d, and Table S3), while MCM-22(60)-5th retained comparable values. These results reveal that moderate Si/Al ratios effectively preserve the pore structure and reduce hydrocarbon residue accumulation, accounting for the superior recyclability and sustained  $C_3H_6/C_3H_8$  separation efficiency of MCM-22(30).

### Dynamic separation and comparison

The dynamic  $C_3H_6/C_3H_8$  separation performance of MCM-22 (*n*) was evaluated in the column breakthrough experiment using a gas mixture with 50%  $C_3H_6$  and 50%  $C_3H_8$  (Figure 6a and Table S4). All samples showed clear separation between the two components. For MCM-22(15),  $C_3H_8$  broke through first at  $\sim 22 \text{ min g}^{-1}$ , followed by a sharp increase in its effluent concentration ( $C/C_0 > 2.0$ ) due to competitive adsorption, whereas  $C_3H_6$  eluted much later ( $\sim 44 \text{ min g}^{-1}$ ). A similar trend was observed for MCM-22(60), where  $C_3H_8$  and  $C_3H_6$  broke through at 26 and 51  $\text{min g}^{-1}$ , respectively (Figure 6a). Remarkably, MCM-22(30) exhibited the best separation behavior, with breakthrough time of 65  $\text{min g}^{-1}$  (for  $C_3H_8$ ) and 151  $\text{min g}^{-1}$  (for  $C_3H_6$ ). The pronounced time delay between the two breakthrough fronts highlights the strong preferential adsorption of  $C_3H_6$  and demonstrates the excellent selectivity of MCM-22(30) under dynamic flow conditions.

A comparative analysis (Figure 6b and Table S5) further benchmarked MCM-22(30) against representative porous adsorbents, including other zeolites, carbon materials, and MOFs. MCM-22(30) surpasses most previously reported adsorbents in both  $C_3H_6$  adsorption capacity and  $C_3H_6/C_3H_8$  selectivity, confirming its superior separation efficiency and potential as a robust, energy-efficient material for olefin/paraffin separations [6,20,52,53].

## CONCLUSIONS

MCM-22 zeolites with tailorable Si/Al ratios were synthesized, and their performance in  $C_3H_6/C_3H_8$

separation was systematically investigated. Structural characterization validated the formation of the typical MWW topology with high crystallinity. Increasing the Si/Al ratio decreases the framework acidity and surface hydroxyl density while enhancing hydrophobicity. Gas adsorption measurements demonstrated that MCM-22(30) with a moderate Si/Al ratio of 18.7 exhibited the highest  $C_3H_6$  uptake of  $6.28 \text{ mmol g}^{-1}$  and  $C_3H_6/C_3H_8$  (50/50,  $v/v$ ) selectivity of 3553 at 298 K. Recycling adsorption-desorption tests revealed the favorable reversibility and structural integrity after multiple cycles. Column breakthrough experiments further evidenced the superior dynamic  $C_3H_6/C_3H_8$  separation over MCM-22(30). This work highlights the great potential of MWW topologic zeolites in the  $C_3H_6/C_3H_8$  separation, with a moderate Si/Al ratio offering the best performance.

## METHOD

### Materials

Silica sol was provided by Guangzhou Yinhan Chemical (China). Sodium hydroxide (NaOH, 96.0 wt%) was offered by Xilong Chemical Reagent Co. (China). Sodium meta-aluminate ( $NaAlO_2$ , 80 wt%) was purchased by Sinopharm Chemical Reagent Co. (China). Hexamethyleneimine (HMI, 99%) was obtained from Sinopharm Chemical Reagent Co. (China).

### Materials synthesis

MWW-type zeolites were synthesized hydrothermally following a modified literature procedure [55]. Typically, NaOH (0.094 g),  $NaAlO_2$  (0.182), silica sol (4.2 g), and HMI (0.9 g) were subsequently dissolved in water (7.738 g), followed by stirring at room temperature for 3 h. The resulting gel with the molar composition of  $1 \text{ SiO}_2:0.11 \text{ Na}_2\text{O}:0.03 \text{ Al}_2\text{O}_3:0.43 \text{ HMI}:20.48 \text{ H}_2\text{O}$  was dynamically crystallized at  $150 \text{ }^\circ\text{C}$  under rotation ( $50 \text{ r min}^{-1}$ ) for 5 d. The solid was recovered by filtration, washed thoroughly with water, and dried to yield as-synthesized MCM-22(15). Calcination was conducted at  $550 \text{ }^\circ\text{C}$  for 5 h. MCM-22(30) and MCM-22(60) were synthesized using the same procedure with the  $NaAlO_2$  feeding of 0.091 and 0.046 g, respectively, to achieve higher Si/Al ratios.

### General characterizations

XRD patterns were collected on a (Rigaku) SmartLab diffractometer with a 9 kW rotating Cu  $K\alpha$  anode (40 kV, 100 mA,  $5^\circ\text{--}50^\circ$ ,  $0.2^\circ \text{ s}^{-1}$ ). FT-IR spectra were measured on an Agilent Cary 660 spectrometer (USA). Morphology was observed with a Hitachi S-4800 (Japan) field emission scanning electron microscope (SEM).  $N_2$  sorption experiment was conducted on a BELSORP-MAX analyzer (Japan) to determine textural parameters. Elemental composition was analyzed by an ADVANT'XP X-ray fluorescence (XRF) spectrometer (ZSX Primus II, Rigaku, Japan). TG analysis was performed on a STA409 equipment (NETZSCH, Germany) under  $N_2$ . The water contact angles on the surface of samples were gauged with a contact angle goniometer (Powereach JC2000, China) equipped with uEye digital camera.

## Gas adsorption

Single-component C<sub>3</sub>H<sub>6</sub> and C<sub>3</sub>H<sub>8</sub> sorption isotherms were measured at 298 and 273 K on a BELSORP-MAX apparatus (Japan). The equilibrium data were fitted using Dual-site Langmuir model, and the C<sub>3</sub>H<sub>6</sub>/C<sub>3</sub>H<sub>8</sub> selectivities are calculated from IAST [49].

## Breakthrough experiments

Breakthrough curves were collected on a custom-built stainless-steel fixed-bed apparatus. The zeolite-packed column (inner diameter: 5 mm; packing length: ~5 cm; zeolite loading: 0.3875 g for MCM-22(15), 0.4107 g for MCM-22(30), and 0.2529 g for MCM-22(60)) was pretreated at 300 °C under vacuum, followed by purging with He (5 mL min<sup>-1</sup>). After that, gas mixture of C<sub>3</sub>H<sub>6</sub>/C<sub>3</sub>H<sub>8</sub> (50/50, v/v) was introduced at a flow rate of 2 mL min<sup>-1</sup>. The effluent composition was continuously monitored by online gas chromatography.

## Data availability

The original data are available from the corresponding authors upon reasonable request.

## Acknowledgements

The computational resources generously provided by the High-Performance Computing Center of Nanjing Tech University are greatly appreciated.

## Funding

This work was supported by the National Natural Science Foundation of China (22222806, 22178162, 22408170, and 22072065), the Distinguished Youth Foundation of Jiangsu Province (BK20220053), the National Key Research and Development Program of China (2024YFE0206900), the Six Talent Peaks Project in Jiangsu Province (JNHB-035), and the State Key Laboratory of Materials-Oriented Chemical Engineering (SKL-MCE-24A06).

## Author contributions

Z.T. and Q.X. contributed to writing the original draft, investigation, and data curation; Y.W., X.S., and X.Z. contributed to data curation; X.L., J.W., and Y.Z. contributed to writing review and editing, supervision, project administration, and funding acquisition.

## Conflict of interest

The authors declare no conflict of interest.

## Supplementary information

The supporting information is available online at <https://doi.org/10.1360/nso/20250064>. The supporting materials are published as submitted, without typesetting or editing. The responsibility for scientific accuracy and content remains entirely with the authors.

## References

- 1 Cui J, Zhang Z, Yang L, *et al.* A molecular sieve with ultrafast adsorption kinetics for propylene separation. *Science*

- 2024; **383**: 179–183.
- 2 Zhang L, Gao R, Liu X, *et al.* Unique H<sub>2</sub>O vortex in one new MOF material strengthening C<sub>3</sub>H<sub>6</sub> adsorption and unprecedented purification from C<sub>2</sub>H<sub>4</sub>/C<sub>3</sub>H<sub>8</sub>/C<sub>3</sub>H<sub>6</sub> mixtures. *Adv Funct Mater* 2025; **35**: 2420927.
  - 3 Ma LL, Liu J, Zhou K, *et al.* A MOF built on 8-connected Y<sub>3</sub> nodes demonstrates simultaneous reverse adsorptive separation: Ethane over ethylene and propane over propylene. *Sci China Chem* 2024; **67**: 3657–3661.
  - 4 Chen XY, Xiao A, Rodrigue D. Polymer-based membranes for propylene/propane separation. *Sep Purif Rev* 2022; **51**: 130–142.
  - 5 Lan T, Yu B, Liu Y, *et al.* Two-dimensional anion-pillared metal-organic framework for sieving separation of propylene from propane with ultrahigh kinetic performance. *Inorg Chem* 2025; **64**: 5322–5330.
  - 6 Dong Q, Huang Y, Wan J, *et al.* Confining water nanotubes in a Cu<sub>10</sub>O<sub>13</sub>-based metal-organic framework for propylene/propane separation with record-high selectivity. *J Am Chem Soc* 2023; **145**: 8043–8051.
  - 7 Ding Q, Zhang S. Recent advances in the development of metal-organic frameworks for propylene and propane separation. *Energy Fuels* 2022; **36**: 7337–7361.
  - 8 Moliner M, Martínez C, Corma A. Synthesis strategies for preparing useful small pore zeolites and zeotypes for gas separations and catalysis. *Chem Mater* 2014; **26**: 246–258.
  - 9 Abbasi S, Khosravi-Nikou MR, Shariati A. Selective separation of propane from the propylene-propane mixture using pure silica zeolites: A molecular dynamic simulation. *Chem Eng Process Int* 2023; **184**: 109294.
  - 10 Jia J, Yan N, Lian X, *et al.* Molecular trapdoor in HEU zeolite enables inverse CO<sub>2</sub>-C<sub>2</sub>H<sub>2</sub> separation. *Angew Chem Int Ed* 2025; **64**: e202419091.
  - 11 Bai R, Song X, Yan W, *et al.* Low-energy adsorptive separation by zeolites. *Natl Sci Rev* 2022; **9**: nwa064.
  - 12 Yue B, Liu S, Chai Y, *et al.* Zeolites for separation: Fundamental and application. *J Energy Chem* 2022; **71**: 288–303.
  - 13 Wang Y, Peh SB, Zhao D. Alternatives to cryogenic distillation: Advanced porous materials in adsorptive light olefin/paraffin separations. *Small* 2019; **15**: 1900058.
  - 14 Wei R, Liu X, Lai Z. MOF or COF membranes for olefin/paraffin separation: Current status and future research directions. *Adv Membr* 2022; **2**: 100035.
  - 15 Xu S, Liu RS, Zhang MY, *et al.* Designed synthesis of porous carbons for the separation of light hydrocarbons. *Chin J Chem Eng* 2022; **42**: 130–150.
  - 16 Zhou Y, Li P, Wang Y, *et al.* Progress in the separation and purification of carbon hydrocarbon compounds using MOFs and molecular sieves. *Separations* 2023; **10**: 543.
  - 17 Tian YJ, Deng C, Peng YL, *et al.* State of the art, challenges and prospects in metal-organic frameworks for the separation of binary propylene/propane mixtures. *Coord Chem Rev* 2024; **506**: 215697.
  - 18 Jeong SR, Park H, Ko Y, *et al.* Adsorption characteristics and separation behavior of binder and binderless zeolite LiX Pellets: O<sub>2</sub>, N<sub>2</sub>, and CO<sub>2</sub>. *Sep Purif Tech* 2025; **355**: 129702.
  - 19 Boer DG, Langerak J, Pescarmona PP. Zeolites as selective adsorbents for CO<sub>2</sub> separation. *ACS Appl Energy Mater* 2023; **6**: 2634–2656.
  - 20 Maghsoudi H, Abdi H, Aidani A. Temperature- and pressure-dependent adsorption equilibria and diffusivities of propylene and propane in pure-silica Si-CHA zeolite. *Ind Eng Chem Res* 2020; **59**: 1682–1692.
  - 21 Moradi H, Azizpour H, Mohammadi M. Study of adsorption of propane and propylene on CHA zeolite in different Si/Al ratios using molecular dynamics simulation. *Powder Tech* 2023; **419**: 118329.
  - 22 Olson DH, Cambor MA, Villaescusa LA, *et al.* Light hydrocarbon sorption properties of pure silica Si-CHA and ITQ-3 and high silica ZSM-58. *Micropor Mesopor Mat* 2004; **67**: 27–33.
  - 23 Khalighi M, Chen YF, Farooq S, *et al.* Propylene/propane separation using SiCHA. *Ind Eng Chem Res* 2013; **52**: 3877–3892.
  - 24 Grande CA, Rodrigues AE. Propane/propylene separation by pressure swing adsorption using zeolite 4A. *Ind Eng Chem Res* 2005; **44**: 8815–8829.
  - 25 Chen Y, Jiang H, Peng Q, *et al.* Successively separating C<sub>3</sub>H<sub>6</sub> and C<sub>2</sub>H<sub>4</sub> from C<sub>2</sub>H<sub>4</sub>/C<sub>2</sub>H<sub>6</sub>/C<sub>3</sub>H<sub>6</sub>/C<sub>3</sub>H<sub>8</sub> mixture in tandem

- fixed beds involving two zeolites LTA well-regulated via low transition-metal doping. *Chem Eng J* 2023; **473**: 145151.
- 26 Kencana KS, Hong SB. Thermodynamic-kinetic synergistic separation of light olefins/paraffins in post-synthetically modified small-pore zeolites. *Small* 2025; **21**: e06212.
- 27 Xiong Y, Tian T, L'Hermitte A, *et al.* Using silver exchange to achieve high uptake and selectivity for propylene/propane separation in zeolite Y. *Chem Eng J* 2022; **446**: 137104.
- 28 Granato MA, Jorge M, Vlught TJH, *et al.* Diffusion of propane, propylene and isobutane in 13X zeolite by molecular dynamics. *Chem Eng Sci* 2010; **65**: 2656–2663.
- 29 Lee HS, Kim NS, Kwon D, *et al.* Post-synthesis functionalization enables fine-tuning the molecular-sieving properties of zeolites for light olefin/paraffin separations. *Adv Mater* 2021; **33**: 2105398.
- 30 Deng G, Cheng K, Meng B, *et al.* Regulating the Si/Al ratio of GIS zeolite with bulky primary particles for selective CO<sub>2</sub> capture from hydrocarbons. *Sep Purif Tech* 2024; **340**: 126764.
- 31 Li Y, Wang Y, Bai H, *et al.* Adjusting the Si/Al ratio of high silica zeolites for efficient ethane and ethylene separation. *Sep Purif Tech* 2024; **336**: 126154.
- 32 Vosoughi M, Maghsoudi H. Characterization of size-selective kinetic-based Ba-ETS-4 titanosilicate for nitrogen/methane separation: Chlorine-enhanced steric effects. *Sep Purif Tech* 2022; **284**: 120243.
- 33 Park J, Cho KH, Kim JC, *et al.* Design of olefin-phobic zeolites for efficient ethane and ethylene separation. *Chem Mater* 2023; **35**: 2078–2087.
- 34 Zhu W, Kapteijn F, Moulijn JA, *et al.* Shape selectivity in adsorption on the all-silica DD3R. *Langmuir* 2000; **16**: 3322–3329.
- 35 Fu H, Qin H, Wang Y, *et al.* Adsorption and separation of *n*/iso-pentane on zeolites: A GCMC study. *J Mol Graphics Model* 2018; **80**: 59–66.
- 36 Akyalçın S, Akyalçın L. Investigation of hydrogen uptake capacity for FAU, MOR, MTW, MWW. *Int J Hydrogen Energy* 2024; **80**: 771–778.
- 37 Zou Z, Kou C, E J, *et al.* Experimental and simulation investigation on the hydrocarbon adsorption performance of the transition metal ion-modified zeolite during cold start process of automotive engine. *Energy* 2025; **330**: 137012.
- 38 Du H, Kalyanaraman M, Cambor MA, *et al.* Hydrocarbon sorption properties of pure silica MCM-22 type zeolite. *Micropor Mesopor Mat* 2000; **40**: 305–312.
- 39 Delitala C, Alba MD, Becerro AI, *et al.* Synthesis of MCM-22 zeolites of different Si/Al ratio and their structural, morphological and textural characterisation. *Micropor Mesopor Mat* 2009; **118**: 1–10.
- 40 Diao D, Zhang H, Wang J, *et al.* Wet-oxidization and exfoliation of non-swollen MCM-22P to dispersible two-dimensional MWW zeolite nanosheets. *Micropor Mesopor Mat* 2022; **330**: 111629.
- 41 Chen JQ, Li YZ, Hao QQ, *et al.* Controlled direct synthesis of single- to multiple-layer MWW zeolite. *Natl Sci Rev* 2021; **8**: nwaa236.
- 42 Sachse A, Aumond T, Rousseau J, *et al.* Impact of hierarchization on the textural properties of MCM-22 based zeolites. *Adv Mater Inter* 2021; **8**: 2100356.
- 43 Li H, Zhang C, Lin Q, *et al.* Epitaxial growth of two-dimensional MWW zeolite. *J Am Chem Soc* 2024; **146**: 8520–8527.
- 44 Shamzhy M, Gil B, Opanasenko M, *et al.* MWW and MFI frameworks as model layered zeolites: Structures, transformations, properties, and activity. *ACS Catal* 2021; **11**: 2366–2396.
- 45 Cao SW, Xiao P, Wang J, *et al.* Active precursor promoting nucleation/growth of MWW zeolite and controlling its morphology. *Pet Sci* 2023; **20**: 1922–1933.
- 46 He WJ, Shen JX, Zhang KB, *et al.* Incorporation of Cu(I) sites into zeolite via a controllable reduction strategy for ethylene/ethane separation. *Inorg Chem* 2025; **64**: 6236–6242.
- 47 Liu S, Wu G, Gong J, *et al.* Synthesis gold and jade type core shell structure Pt@Sn in deboronated MWW zeolite and its good performance for light alkane dehydrogenation. *Chem Eng J* 2023; **476**: 146410.
- 48 Li Q, Cong W, Li K, *et al.* Transformation synthesis of SSZ-13 zeolite from ZSM-35 zeolite. *J Solid State Chem* 2021;

- 304:** 122635.
- 49 Zhou Y, Hu W, Xi S, *et al.* Mn-doped Y zeolite for ethylene/acetylene separation. *Chem Eng Sci* 2025; **316**: 121960.
- 50 Min JG, Kemp KC, Hong SB. Propylene/propane separation on a ferroaluminosilicate levynite zeolite. *Micropor Mesopor Mat* 2020; **294**: 109833.
- 51 Zhou Y, Zhang J, Wang L, *et al.* Self-assembled iron-containing mordenite monolith for carbon dioxide sieving. *Science* 2021; **373**: 315–320.
- 52 Wang CT, Li WC, Wang M, *et al.* Wood-structured carbon with reassembled pores showing high propylene adsorption rate for efficient separation of propylene/propane. *Sep Purif Tech* 2025; **354**: 128649.
- 53 Gi Min J, Christian Kemp K, Kencana KS, *et al.* Dealuminated Cs-ZK-5 zeolite for propylene/propane separation. *Chem Eng J* 2021; **413**: 127422.
- 54 Koudelková E, Ghrib Y, de Oliveira Ramos FS, *et al.* Adsorption and separation of the C3 hydrocarbons on cationic FER zeolites: Effect of dual sites existence. *Micropor Mesopor Mat* 2019; **279**: 416–422.
- 55 Tuo J, Sheng Z, Gong X, *et al.* Shape-selective synthesis of *para*-xylene through tandem CO<sub>2</sub> hydrogenation and toluene methylation over ZnCeZrO/MCM-22 catalyst. *Chin J Catal* 2025; **73**: 174–185.